Article

Microwave Antenna Sensor with Machine Learning for Non-Destructive Detection of Fresh Meat

Guoping Hu, Lin He, Guolong Shi, Fanli Meng, Yigang He

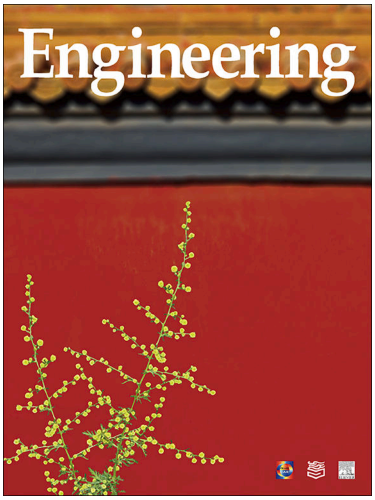

PII: S2095-8099(26)00123-2
DOI: https://doi.org/10.1016/j.eng.2026.01.028
Reference: ENG 2278

To appear in: *Engineering*

Received Date: 31 May 2025
Revised Date: 16 December 2025
Accepted Date: 5 January 2026

Please cite this article as: G. Hu, L. He, G. Shi, F. Meng, Y. He, Microwave Antenna Sensor with Machine Learning for Non-Destructive Detection of Fresh Meat, *Engineering* (2026), doi: https://doi.org/10.1016/j.eng.2026.01.028

Research

Agricultural Sensors—Article

Microwave Antenna Sensor with Machine Learning for Non-Destructive Detection of Fresh Meat

Guoping Hu [a], Lin He [a], Guolong Shi [a,b,*], Fanli Meng [c], Yigang He [d]

[a] *School of Information and Artificial Intelligence, Anhui Agricultural University, Hefei 230036, China*

[b] *Key Laboratory of Agricultural Sensors (Ministry of Agriculture and Rural), Hefei 230036, China*

[c] *School of Information Science and Engineering, Northeastern University, Shenyang 110819, China*

[d] *School of Electrical Engineering and Automation, Wuhan University, Wuhan 430072, China*

* Corresponding author.

E-mail address: shigl@ahau.edu.cn (G. Shi)

ARTICLE INFO

Article history:

Received

Revised

Accepted

Available online

Keywords:

Fresh meat

Detection of quality deterioration

Temperature and humidity compensation

Backpropagation neural network–Pearson correlation analysis

ABSTRACT

The quality of fresh meat inevitably deteriorates during refrigerated storage, and ammonia is a critical volatile marker of spoilage. Nevertheless, temperature and humidity fluctuations within the cold chain environment can decrease the reliability of ammonia detection. To overcome this limitation and increase the sensing precision, in this work, a microwave ammonia sensor with temperature and humidity compensation is proposed on the basis of a backpropagation (BP) neural network. By analyzing the correlation between the radiation gain of the sensor and the ammonia concentration and integrating a wireless power transmission model, a new wireless microwave ammonia sensing model was established. The sensing system was experimentally validated through real-time monitoring of ammonia released during the spoilage of refrigerated meat. The results indicate that BP neural network-based temperature and humidity (THBP) compensation with Pearson correlation analysis reduced the radio frequency signal zero-point frequency fluctuation by 14 MHz, limited the absolute error to 0.06 parts per million (ppm), and increased the detection accuracy by 31.11%. This work provides a reliable theoretical framework and practical approach for high-sensitivity, non-destructive monitoring of the quality of fresh meat in dynamic cold-chain.

1. Introduction

Owing to increasing public concerns about food safety and health, monitoring the quality of fresh agricultural products has become a critical aspect of the food supply chain. Consumers are increasingly willing to pay higher prices to ensure food safety, with a significant portion allocated to food and agricultural product testing [1,2]. Owing to their perishable nature and high dependence on storage conditions, the quality of fresh agricultural products often deteriorates during transportation, storage, and sales. In particular, fluctuations in temperature, humidity, and gas composition during cold chain logistics management directly affect product quality [3]. Ammonia, an important indicator gas in the spoilage process of fresh agricultural products, is closely associated with product quality deterioration. Furthermore, ammonia is also crucial in environmental quality assessment and food safety traceability [4]. Therefore, real-time monitoring of the ammonia concentration provides not only an effective early warning of quality changes in agricultural products but also offers critical data for quality assurance in cold chain logistics management. Researchers worldwide have conducted extensive studies on the quality detection of fresh agricultural products, focusing on techniques such as hyperspectral imaging [5], impedance-based electronic noses [6], Raman spectroscopy [7], optical sensors [8], and gas sensors [9] to detect toxic gases or volatile organic compounds (VOCs) generated during spoilage. Although these technologies have achieved significant progress in agricultural product quality monitoring, their practical applications are limited by complex sample preparation, high costs, and the need for specialized operation [10].

Recently, microwave gas sensors (MGSs) have been thoroughly evaluated in the field of gas sensing because of their high sensitivity, ease of fabrication, and nondestructive detection capabilities [11]. While they operate within the frequency range of 300 MHz to 300 GHz, the electromagnetic fields and sensor characteristics of MGSs change according to the material properties [12]. When the sensor is loaded with the material that is being tested, the sensitive material interacts with the target gas through adsorption and reaction. By recording changes in the transmitted or reflected frequency response, real-time detection of the gas concentration can be achieved [13–15]. Although significant progress in gas detection has been made using microwave sensors, the combined effects of various environmental factors on their performance still require further investigation [16].

Owing to the complexity of gas sensor working mechanisms and their wide range of applications, several challenges remain [17]. For example, environmental factors such as temperature, humidity, air pressure, and wind direction often cause frequency drift, thereby affecting the accuracy of gas detection. Under extreme conditions, sensors may experience zero-point frequency shifts, where differences in frequency occur even when the target gas is not present, significantly reducing detection precision [18]. Consequently, effectively mitigating the interference caused by these environmental variables to increase the precision of sensing remains an important research focus. In terms of gas sensor design, common strategies for decreasing humidity-induced perturbations involve the incorporation of hydrophobic coatings or waterproof encapsulation to suppress water molecule adsorption on sensitive material surfaces [19]. In terms of temperature compensation, widely used techniques include calibration via bridge circuits or feedback control mechanisms [20]. However, these strategies have drawbacks, such as reduced gas-sensing performance and an increase in the overall sensor size. Currently, analyzing the effect of temperature and humidity on gas sensors from experimental data and exploiting these insights for compensation have become feasible and effective strategies [21,22].

To address the demand for high-precision detection of volatile ammonia associated with quality deterioration in fresh meat during storage and transportation, a chipless microwave ammonia sensor integrated with a BP neural network-based temperature and humidity (THBP) compensation algorithm was developed. By analyzing the correlation between the radiation gain of the sensor and ammonia concentration, and integrating a wireless power transmission model, a new wireless microwave ammonia sensing model was established. Experimental validation was performed in refrigerated environments to monitor volatile ammonia released during the spoilage process of fresh meat. The results revealed that fluctuations in temperature and humidity caused significant shifts in the zero-point frequency of the radio frequency signal, which substantially reduced the accuracy of ammonia detection. After the proposed THBP compensation–Pearson correlation analysis algorithm was applied, the concentration prediction error was reduced to 0.06 parts per million (ppm), and the detection accuracy increased by 31.11%.

2. Materials and methods

2.1. Microwave sensor simulation and design

In this study, the crossed split ring resonator (CSRR)-based sensing resonator is excited by a microstrip transmission line, as shown in Fig. 1(a). To facilitate measurement, the microstrip transmission line is designed in a U-shaped structure, which ensures that the transmission line ports of the CSRR are positioned on the same side. The substrate material is flame retardant 4 (FR4) with a relative permittivity of 4.4 and dimensions of 50 mm × 29 mm × 1.6 mm. To improve the performance of the microstrip resonator, a symmetric design, in which two CSRR structures are symmetrically arranged on both sides of the microstrip line to achieve common-mode resonance suppression, is employed [23]. Owing to its asymmetric distribution, a single CSRR structure tends to excite common-mode currents at specific frequencies, resulting in increased electromagnetic interference, reduced signal integrity, and decreased filtering and sensing performance. The symmetric CSRR structure effectively suppresses common-mode resonance by symmetrically loading resonant units on both sides of the microstrip line, ensuring a balanced distribution of common-mode current paths. This arrangement creates a phase cancellation effect, reducing the common-mode resonance peak, improving electromagnetic coupling, and increasing microstrip signal transmission efficiency. As shown in Fig. 1(b), electromagnetic simulation and radio frequency signal measurements reveal that the symmetric CSRR microstrip resonator achieves a higher transmission coefficient (S_{21}), indicating better transmission efficiency, and a stronger electromagnetic field intensity at the resonator opening. The equivalent circuit model of the CSRR-based sensor is shown in Fig. 1(c), where L represents the equivalent inductance of the microstrip line, and C_1 denotes the coupling strength between the microstrip line and the resonator. The coupling strength is effected by the distance between the microstrip line and the resonant ring, which affects the resonance frequency. The resonance frequency f_n of S_{21} can be calculated with Eq. (1), where C_n and L_n represent the equivalent components of the CSRR and primarily determine the bandstop resonance frequency. Additionally, the sensor incorporates a sensitive material (modeled as a variable capacitor C_2), resulting in a microstrip resonator model that responds to changes in the loaded sensing material.

$$f_n = \frac{1}{2\pi\sqrt{L_n C_n}} \qquad (1)$$

Through structural parameter optimization and simulation, the effect of microstrip resonator parameters on impedance matching was systematically analyzed. The compact design of the CSRR, enables the use of a Smith chart to evaluate impedance matching across different dimensions (L, W, and W_1) (Fig. 1(d)). Extensive parametric simulations revealed that optimal impedance matching occurs at L = 12 mm, W = 16 mm, and W_1 = 1 mm, with an impedance value of 1.0016–0.0005i. To further investigate the effect of structural parameters on the transmission coefficient S_{21}, a controlled variable method was applied. As shown in Fig. 1(e), a frequency sweep was conducted by changing the CSRR open-ring gap (X_G) from 2 to 6 mm in 1 mm increments. The results indicate that as X_G increases, the resonance frequency of S_{21} increases. Similarly, the effect of the gap (S) between the CSRR and the microstrip line was examined by sweeping S from 0.25 to 1 mm in 0.25 mm increments (Fig. 1(f)). The findings reveal that a larger S results in an increased resonance frequency of S_{21}. On the basis of these simulation results, the relationship between the microstrip resonator dimensions and S-parameters was established, enabling the design of an optimized microstrip resonator. When the CSRR-to-microstrip line gap S = 0.5 mm, the electric field coupling reaches its peak, significantly increasing the coupling strength of the resonator. This results in a stronger electromagnetic interaction between the CSRR and the microstrip line, increasing the signal transmission efficiency and absorption capacity.

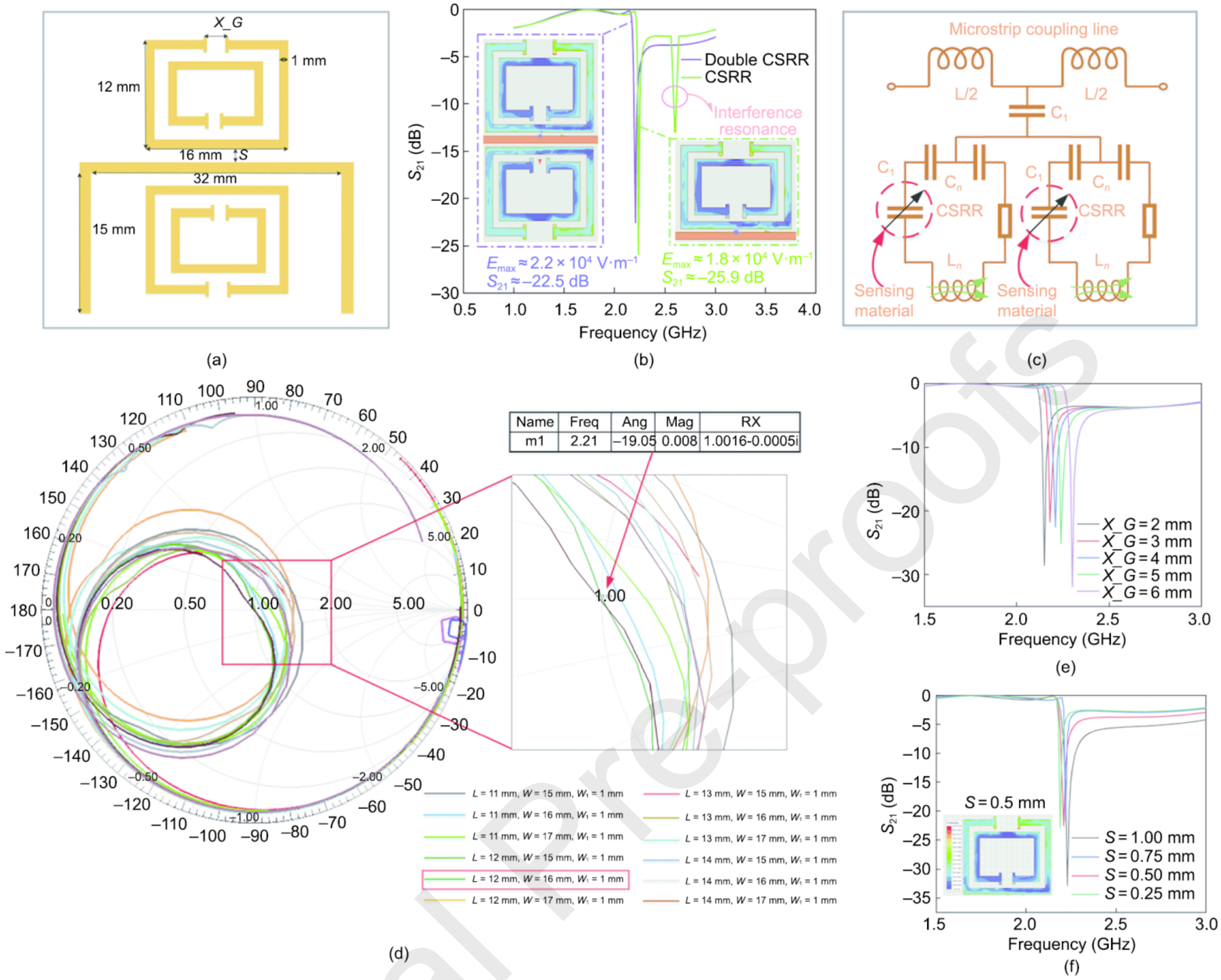

Fig. 1. (a) Schematic of the sensor structure, (b) performance comparison between a symmetric CSRR and a single CSRR, (c) equivalent circuit model, (d) Smith chart of impedance matching for the microstrip resonator, (e) variation in S_{21} with *X_G*, (f) variation in S_{21} with *S*. E_{max}: maximum electric field; Freq: frequency; Ang: angle; Mag: magnitude; RX: resistance and reactance; C: capacitor; L: inductor.

2.2. Characterization of gas-sensitive materials

Single-walled carbon nanotubes (SWCNTs) have excellent ammonia adsorption properties, primarily because of their high specific surface area, π-conjugated electronic structure, and tunable surface chemistry [24,25]. With respect to SWCNTs, the G-band has two main peaks: G^- (1573.20 cm^{-1}) and G^+ (1595.62 cm^{-1}). The G^- mode reflects circumferential vibrations and shifts to lower frequencies with decreasing diameter, indicating that the nanotubes in this study are semiconducting with a bandgap sensitive to gas adsorption. The G^+ mode corresponds to axial vibrations and its frequency is related to the electronic structure, which is useful for assessing conductivity. As shown in Fig. 2(a), the D-band at 1341.36 cm^{-1} stems from structural defects; its low intensity here suggests high-quality nanotubes with minimal defects, which are favorable for charge transport and sensing. The radial breathing mode (RBM) at 159.12 cm^{-1} corresponds to radial atomic motions; its low frequency indicates a larger diameter, providing greater surface area for gas adsorption and improved sensitivity. The G' band (2D band) at 2670.38 cm^{-1}, a second-order overtone of the D-band (Fig. 2(b)), provides further insight into the electronic band structure.

To investigate the microstructure of the material, transmission electron microscopy (TEM) was employed, as shown in Fig. 2(c). At low magnification, the SWCNTs have a typical one-dimensional tubular morphology, arranged in parallel bundles or interwoven networks, with uniform diameters of 1–2 nm and lengths extending to the micrometer scale. High-magnification images clearly reveal their hollow cylindrical structure, with the graphene layers spirally wrapped along the axis, forming tube walls with an interlayer spacing of 0.34, which is consistent with the theoretical values. The observed bending morphology reflects excellent flexibility and mechanical strength, owing to the stable hexagonal network of sp^2-hybridized carbon atoms. High-resolution images also reveal localized lattice distortions labeled “defects,” which are likely caused by chemical etching, mechanical stress, or growth defects. These defects may serve as stress concentration sites and modulate the electronic density of states, potentially increasing ammonia sensitivity.

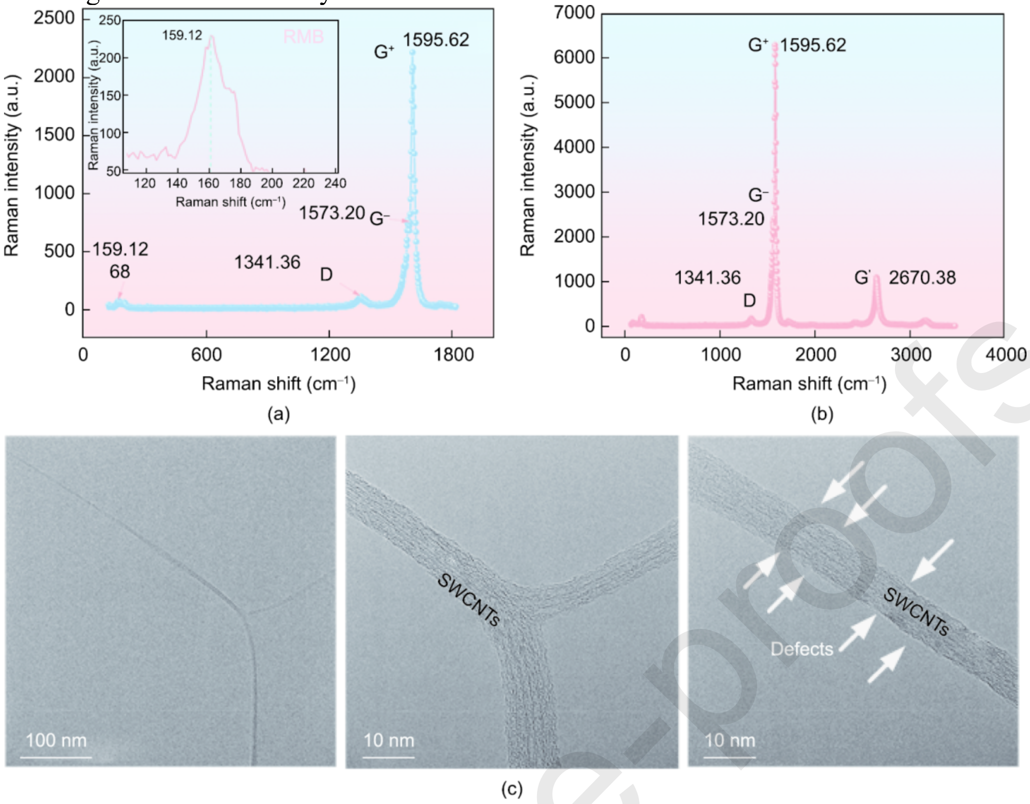

Fig. 2. (a, b) Raman characterization of SWCNTs, (c) TEM characterization of SWCNTs.

2.3. Sensing method and mechanism

According to perturbation theory [26], the electromagnetic field intensity within the sensitive region is closely related to changes in the electromagnetic properties of the material. These factors jointly induce a perturbation response, which is reflected as changes in the resonant frequency and amplitude of the *S*-parameters. Consequently, concentrating an increased electromagnetic field in the sensitive region can significantly increase the sensitivity of the MGS, thereby improving gas detection performance [27]. In this study, simulation and experimental analyses are used to investigate the electromagnetic field distribution in the sensitive region and its interaction with variation in dielectric loss induced by gas adsorption (Fig. 3(a)).

Electromagnetic simulation analysis reveals that in the rectangular CSRR, the electric field intensity is strongest at the opening of the outer ring, whereas the magnetic field intensity peaks at the opening of the inner ring. On the based of the results of the NH_3 adsorption experiments, when the NH_3 molecules adsorb onto the SWCNT surface, electron transfer occurs from the NH_3 molecules to the SWCNT surface. This reduces the hole concentration of free surface electrons, causing partial electron trapping or release, which results in the formation of electron or hole traps. Under an external electric field, these trapped carriers are excited into the conduction or valence band, and converted into free carriers. As the free carrier concentration increases, the loss of conductivity also increases, increasing the overall dielectric loss. Furthermore, the generation of trap states and the excitation of charge carriers result in frequent or unstable polarization responses, further increasing dielectric loss. As shown in Fig. 3(b), when SWCNTs are loaded into the region with the strongest electric field, the resonance frequency increases with increasing dielectric loss tangent, significantly affecting S_{21}. Conversely, as shown in Fig. 3(c), when SWCNTs are loaded into the region with the strongest magnetic field, the effect of magnetic loss tangent on the resonance frequency is minimal, with only slight fluctuations in the S_{21} amplitude. Therefore, coating SWCNTs in the strong electric field region of the microstrip resonator effectively increases the detection signal.

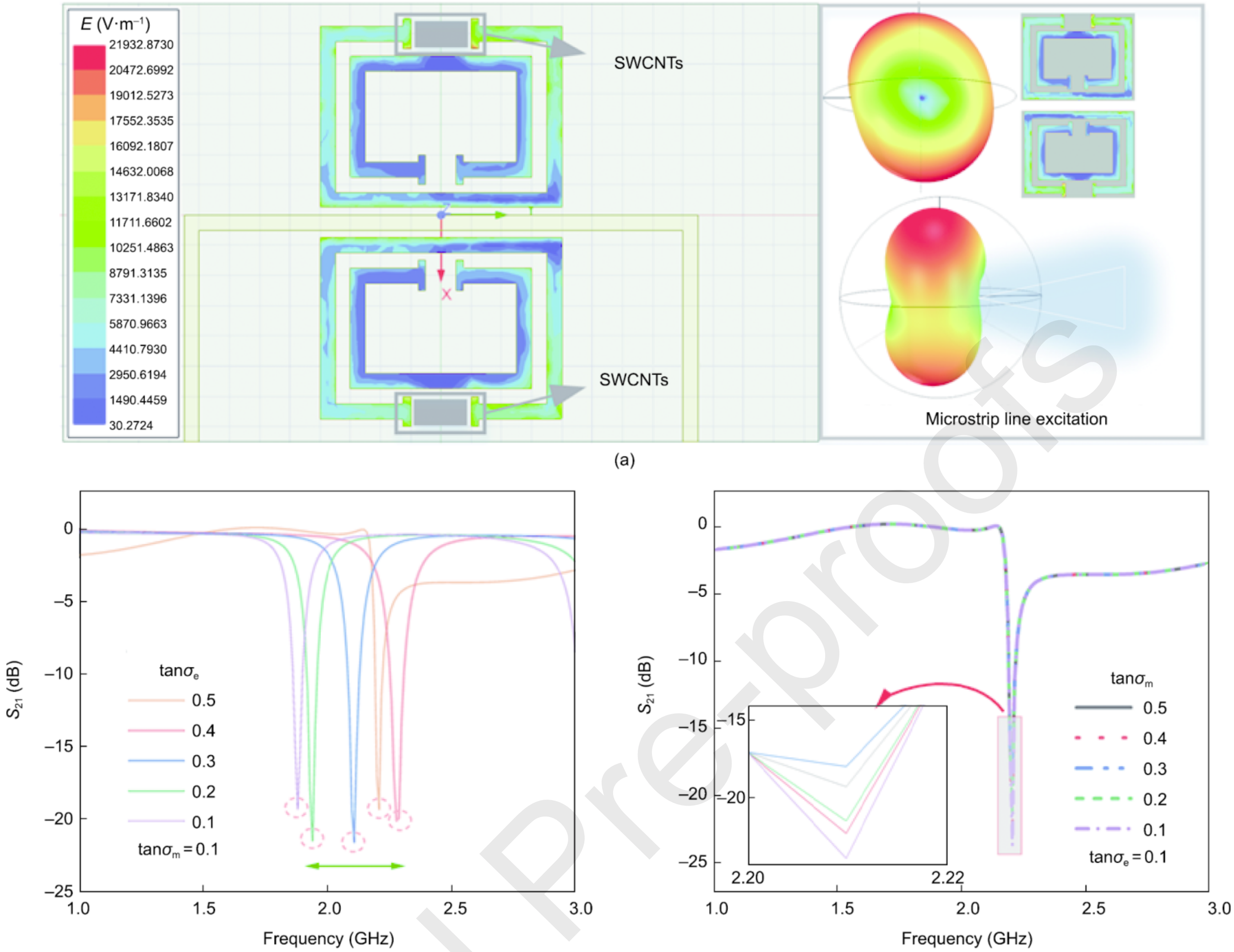

(a)

(b)

(c)

Fig. 3. (a) Simulation of the interaction between the sensing material and the electromagnetic field, (b) variation in the dielectric loss under a strong electric field, (c) variation in the dielectric loss under a strong magnetic field. *E*: electric field strength; σ_e: electric loss angle; σ_m: magnetic loss angle; S_{21}: transmission coefficient.

SWCNTs, typical p-type semiconductors, have a significantly higher hole concentration than electron concentration. As shown in Fig. 4(a), the sensing mechanism of the microwave ammonia sensor relies on the adsorption-induced modulation of the electronic structure and conductivity of the SWCNTs. When ammonia molecules are adsorbed onto the SWCNT surface, electron donation from ammonia reduces the hole concentration, causing a decrease in conductivity and a corresponding increase in resistance. Owing to their strong polarity, ammonia molecules exhibit increased adsorption via dipole–dipole, dipole-induced dipole, and π–π interactions involving nitrogen lone pair electrons, facilitating stable anchoring on the SWCNT surface. This process is further accompanied by increased van der Waals forces and the formation of a space charge region, resulting in an upward shift in the Fermi level and widening of the valence band gap, both of which facilitate reduced carrier mobility and conductivity. During ammonia adsorption, the transfer of free electrons reduces the hole concentration in SWCNTs, decreasing their conductivity but increasing resistance.

During desorption, electrons flow back to the ammonia molecules, causing the resistance to recover. The impedance matching of the microwave antenna sensor is achieved through the synergistic interaction between the microstrip resonator and the gas-sensitive material. The adsorption and desorption of ammonia dynamically change the resistance of SWCNTs, which affects the impedance matching between the microstrip resonator and the sensitive layer (Eq. (2)). Increased impedance mismatch results in greater signal reflection, altering the amplitude and resonance frequency of the S_{21} parameter of the sensor (Eq. (3)). The S_{21} value reflects the efficiency of microwave signal transmission, and its variation is highly correlated with the ammonia concentration, enabling real-time quantitative detection of ammonia.

$$Z_{in} = R + jX \qquad (2)$$

$$S_{21} = \frac{2Z_0}{Z_{in}+Z_0} \qquad (3)$$

where Z_{in} represents the input impedance, Z_{o} denotes the characteristic impedance, R indicates the resistance component, j represents the imaginary unit, and X represents the reactance component.

2.4. Electrical measurements

As shown in Fig. 4(b), the experimental system is composed of the following components: a vector network analyzer (VNA), a spectrum analyzer, a reaction chamber (dimensions: 30 cm × 20 cm × 25 cm), a temperature control system (including ice packs and heating wires), a laptop computer, a ultra-wideband dipole (UWB-4) receiving antenna, standard gas cylinders, a vacuum pump, and a temperature-humidity meter. Under the control of a gas mixing program, a high-precision mass flow controller is used to accurately regulate the flow rates of standard gases, ensuring thorough mixing of the background gas nitrogen (N_2) and the target gas ammonia (NH_3) within the gas measurement chamber. The NH_3 concentration is calculated using Eq. (4) [28], where C_{b} represents the concentration of the stock gas, and V_1 and V represent the injected volume and the chamber volume, respectively. In the temperature and humidity interference analysis experiments, the temperature is regulated within the range of 5–25 °C, and the relative humidity is controlled between 40%–80% to simulate the effects of various environmental conditions on sensor performance. During the experiment, the interfering gases in the reaction chamber are evacuated, and then the pre-calibrated ammonia mixture is added. The temperature and humidity conditions are adjusted to assess the detection performance of the sensor across different NH_3 concentrations. After each test, the remaining gas in the reaction chamber is evacuated and replaced with a new NH_3 mixture, and the experimental cycle continues until measurements under all temperature and humidity conditions are completed.

$$C = (V_1 \times C_b)/V \qquad (4)$$

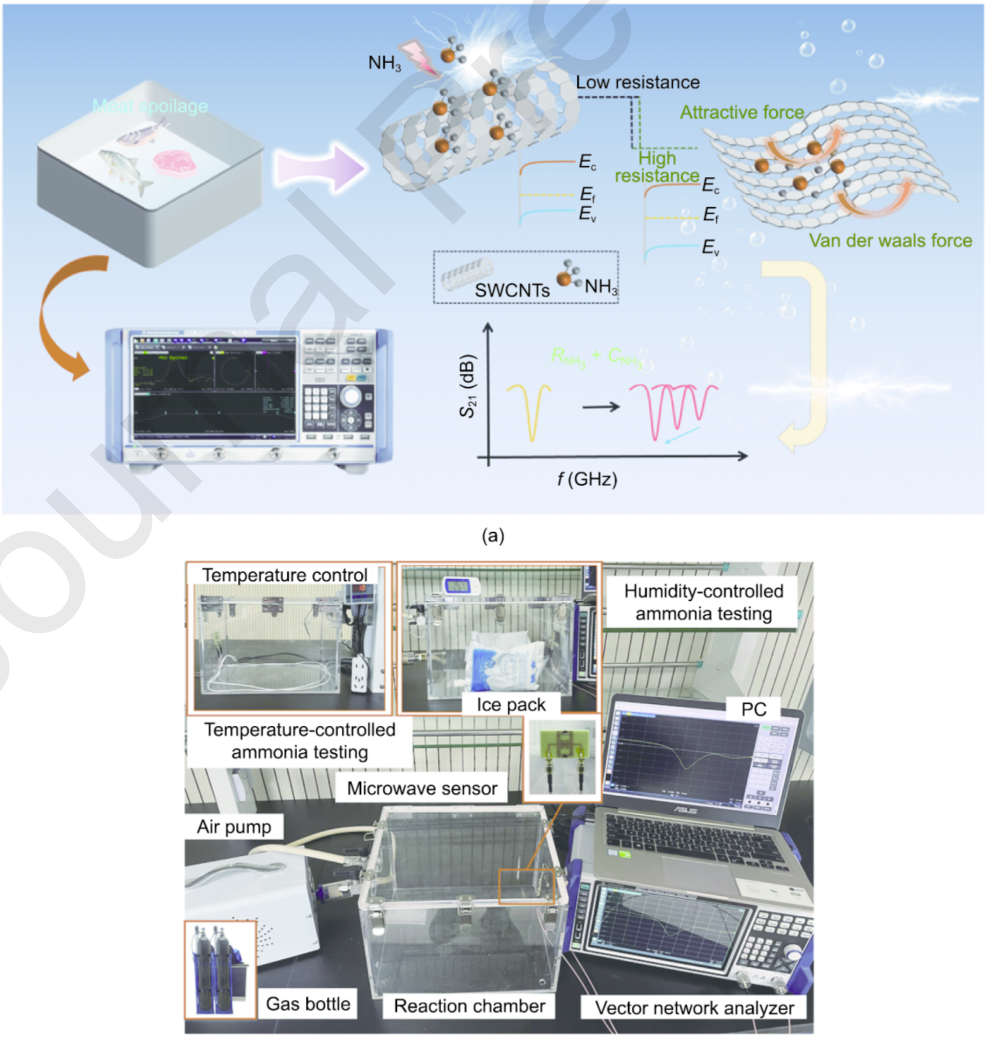

(a)

(b)

Fig. 4. (a) Ammonia sensing mechanism, (b) setup of the electrical measurement system. S_{21}: transmission coefficient; NH_3: ammonia; f: frequency; E_c: conduction band minimum; E_v: valence band maximum; E_f: fermi level; PC: personal computer.

3. Results and analysis

3.1. Sensing performance analysis

In accordance with the electrical measurements shown in Fig. 5, the microwave sensor was placed in a sealed reaction chamber to investigate the variation in S_{21} in an ammonia environment with concentrations ranging from 5 to 20 ppm. As shown in Fig. 5(a), the resonance frequency of the microwave sensor gradually decreases with increasing ammonia concentration, with a total shift of approximately 45 MHz and a sensitivity of 3 $\text{MHz}\cdot\text{ppm}^{-1}$. The linear fitting curve of the response of the sensor within the range of 5–20 ppm NH_3 is shown in Fig. 5(b), which reveals a strong correlation between the frequency shift and the NH_3 concentration ($R^2 = 0.9673$). This finding further validates the relationship between ammonia adsorption and the frequency variation of the sensor. A network analyzer was used to perform a far-field analysis of the microwave sensor. The two-dimensional radiation gain distribution and peak gain at different ammonia concentrations are shown in Figs. 5(c) and (d). As the ammonia concentration increases, the degree of impedance matching decreases, resulting in a decrease in peak gain. Consequently, the relationship between the radiation gain (G_{MGS}) and concentration (Conc.) is established.

$$G_{MGS} = a * \text{Conc.} + b \qquad (5)$$

where a and b are the respensent correlation coefficients of the microwave sensor. On basis of the correlation study between the ammonia concentration and sensor radiation gain, the values were determined to $a = -0.177$ and $b = -10.612$.

To validate the repeatability of the microwave sensor, five repeated tests were performed under identical conditions, and the resonance frequency shift and response behavior of the sensor were measured at different time intervals. As shown in Fig. 5(e), the sensor response percentage stabilized at 22% approximately 24 s after ammonia adsorption and recovered to its initial value approximately 27 s after desorption. The high consistency across the three experimental results confirms the excellent repeatability of the sensor. In accordance with Eqs. (6)–(8) [29], the measured S_{21} values were converted into sensor response percentages.

$$\%Sensorresponse = \frac{|\triangle S_{21}|}{|S_{21,air}|} \times 100, \qquad (6)$$

$$|\triangle S_{21}| = \begin{Bmatrix} [\,Re(S_{21})_{air+NH_3} - Re(S_{21})_{air}]^2 \\ +[\,Im(S_{21})_{air+NH_3} - Im(S_{21})_{air}]^2 \end{Bmatrix}^{\frac{1}{2}} \qquad (7)$$

$$|\triangle S_{21,air}| = \{[nRe(S_{21})_{air}]^2 + [Im(S_{21})_{air}]^2\}^{\frac{1}{2}}. \qquad (8)$$

The real part of the S_{21} parameter of the sensor in air and ammonia, the real part of the S_{21} parameter of the sensor in air, the imaginary part of the S_{21} parameter of the sensor in air and ammonia, and the imaginary part of the S_{21} parameter of the sensor in air are denoted as $\text{Re}(S_{21})_{\text{air+NH3}}$, $\text{Re}(S_{21})_{\text{air}}$, $\text{Im}(S_{21})_{\text{air+NH3}}$, and $\text{Im}(S_{21})_{\text{air}}$, respectively. The labeled S_{21} value in air is represented by $|S_{21}, \text{air}|$, the absolute value of the change in the labeled S_{21} coefficient because of ammonia adsorption, which is represented by $|\Delta S_{21}|$. Eq. (6) is directly correlated with the percentage of the sensor response.

Furthermore, gas selectivity is a key factor in evaluating the practical performance of a sensor. As shown in Fig. 5(f), selectivity analysis was conducted under the same conditions for four gases commonly produced during agricultural product spoilage (C_3H_6, C_2H_4, CO_2, and H_2S) [30]. A multimeter was used to monitor the resistance variation of the sensor during the adsorption of different gases, revealing only minor resistance changes for the four interfering gases. Moreover, compared with the sensor response percentage observed during ammonia adsorption, the response percentages for the interfering gases were negligible. This finding that the sensor exhibits significant selectivity toward ammonia, with minimal cross-sensitivity to interfering gases.

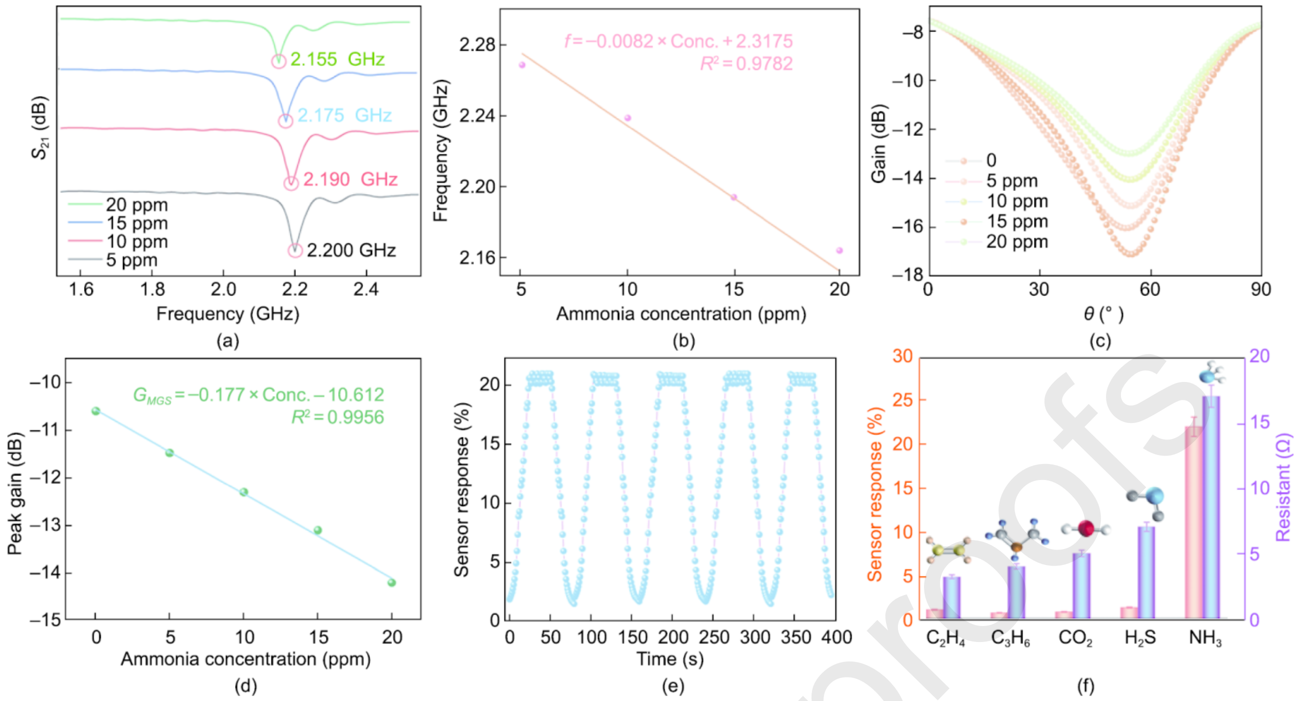

Fig. 5. (a) variation in the S_{21} parameter induced by ammonia adsorption, (b) linear regression analysis of ammonia adsorption, (c) two-dimensional radiation gain distribution of the microwave sensor, and (d) peak gain response under different ammonia concentrations, (e) repeatability assessment of the sensor, (f) gas selectivity evaluation. G_{MGS}: the radiation gain of MGS; Conc.: concentration; R: the related coefficient.

3.2. Gas chromatographic analysis of volatile compounds in fresh meat with quality deterioration

To elucidate the physicochemical characteristics underlying the sensory changes, gas chromatography–mass spectrometry (GC–MS) analysis was performed on the volatile compounds of fresh meat stored at 5 °C for 48 and 72 h. The experimental setup consists of a syringe, gas sampling bag, connector, and tubing. Fresh meat samples are placed in a sealed container and allowed to undergo natural spoilage. Volatile compounds released during the decomposition process are extracted from the container using a syringe. The syringe is connected to the gas sampling bag via a connector and tubing, and the extracted gases are transferred into the bag. The collected gas samples are analyzed using gas chromatography. As shown in Fig. 6(a), the sensory properties of the meat significantly changed with prolonged storage: the color gradually shifted from bright red to dark red. The results of GC–MS revealed that the chromatographic peak intensities of typical volatile gases, such as carbon dioxide, ammonia, hydrogen sulfide, and methane, increased gradually, indicating a significant increase in gas concentration during the spoilage process (Fig. 6(b)). These compounds were closely correlate with the observed sensory deterioration, suggesting that changes in physicochemical indicators can effectively reflect the decrease in meat quality.

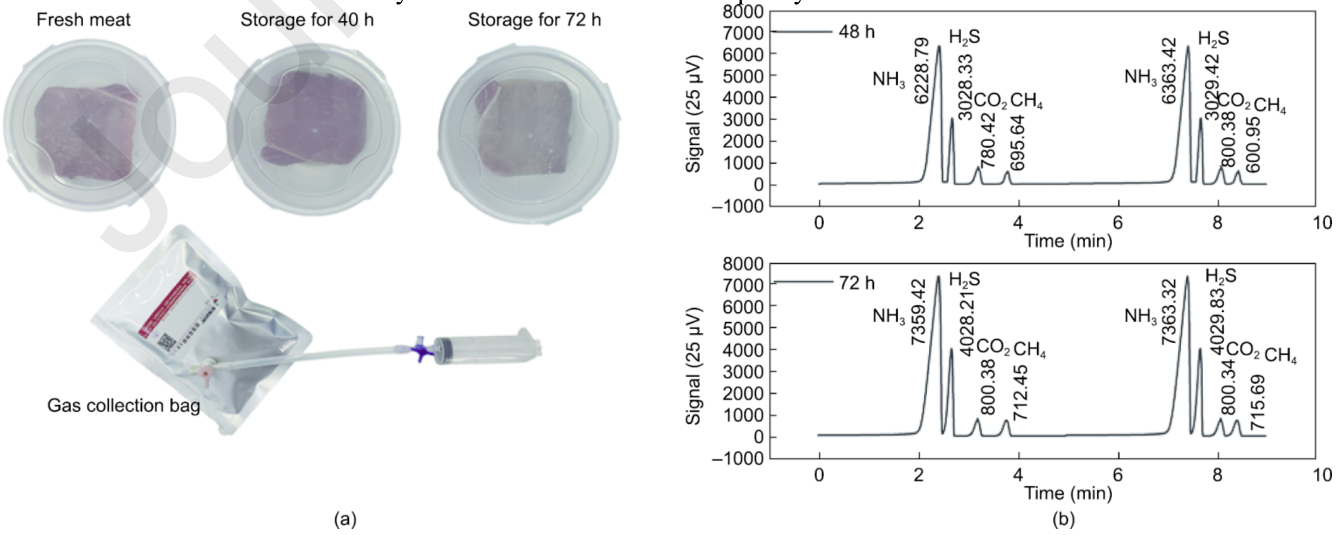

Fig. 6. (a) Sensory analysis of quality changes in chilled fresh meat during cold storage, (b) GC–MS analysis of volatile compounds.

3.3. Analysis of temperature and humidity interference

To investigate the relationships between the environmental temperature and humidity and the zero-point frequency shift of the microwave gas sensor, a 7 d data collection experiment was conducted under simulated real-world conditions. To reduce the effect of random factors, the zero-point frequency shifts of four identical microwave sensors (S1, S2, S3, and S4) were recorded under the same conditions. The measured zero-point frequency shift corresponds to the S-parameters converted from radio frequency electromagnetic waves, with the frequency shift unit expressed in Hz. The experiment was performed in an interference-free environment to eliminate the effect of nontarget gases on the baseline frequency signal of the sensor. During data collection, the temperature ranged from 5−25 °C, and the relative humidity ranged between 40% and 80%. As shown in Figs. 7(a) and (b), a controlled variable method was employed to analyze the effects of temperature and humidity on the zero-point frequency shift [31–33].

During actual measurements, as the temperature decreased from 25 to 5 °C and the relative humidity increased from 40% to 80%, the sensor exhibited a frequency shift of 60 MHz in an ammonia concentration range of 5–20 ppm, resulting in a sensitivity of 4 MHz·ppm^{-1}. Compared with the indoor environment sensitivity of 3 MHz·ppm^{-1}, the sensitivity error increased by a factor of 1.33. To further validate the effect of temperature and humidity on the performance of the ammonia gas sensors (Fig. 7(c)), this study employed Pearson correlation analysis to evaluate the relationships between four sensors (S1, S2, S3, and S4) and environmental variables, namely temperature (T) and relative humidity (RH). The correlation coefficients are shown in Fig. 7(d), where $|P| < 0.4$ indicates weak correlation and $|P| > 0.4$ indicates a significant correlation. Statistical results indicate that the average correlation coefficient for temperature interference is $|P| = 0.56$, and with respect to humidity interference, $|P| = 0.45$, suggesting that both temperature and humidity have a notable effect on sensor performance.

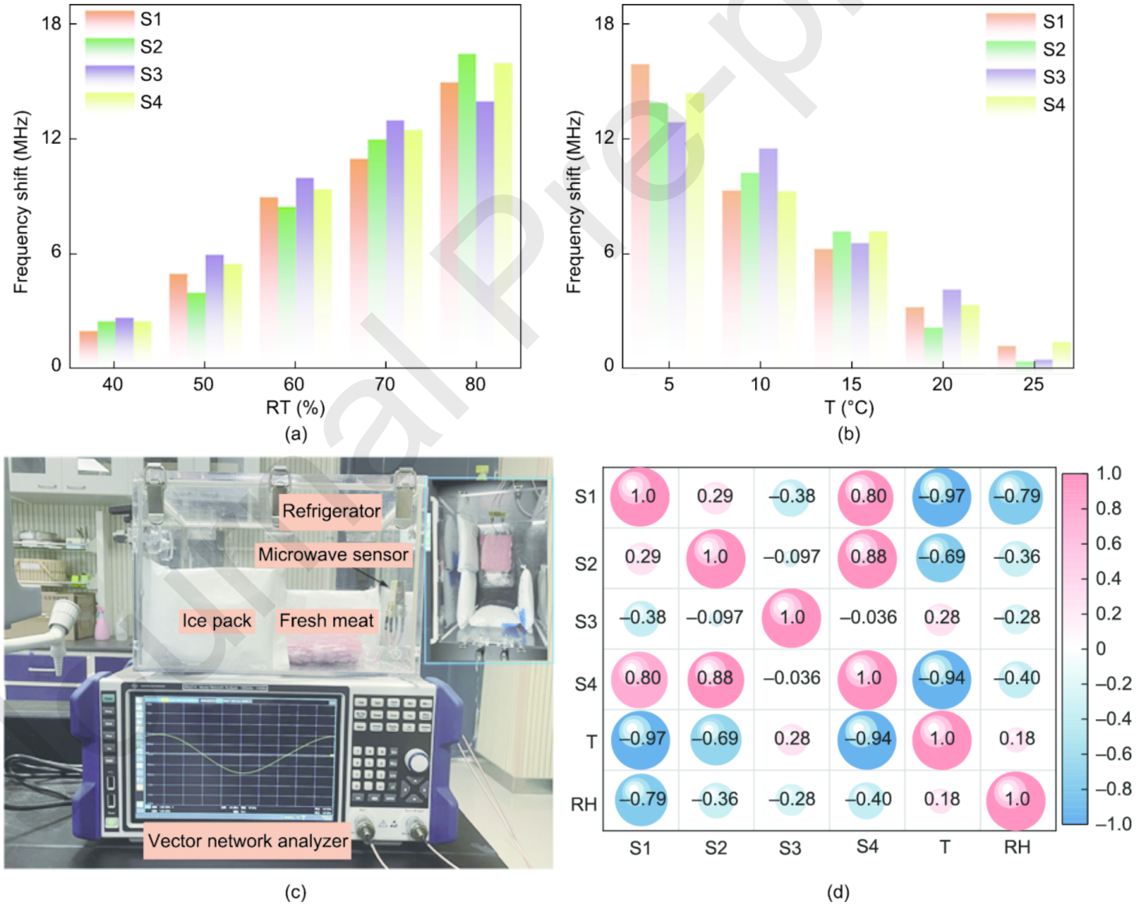

	S1	S2	S3	S4	T	RH
S1	1.0	0.29	−0.38	0.80	−0.97	−0.79
S2	0.29	1.0	−0.097	0.88	−0.69	−0.36
S3	−0.38	−0.097	1.0	−0.036	0.28	−0.28
S4	0.80	0.88	−0.036	1.0	−0.94	−0.40
T	−0.97	−0.69	0.28	−0.94	1.0	0.18
RH	−0.79	−0.36	−0.28	−0.40	0.18	1.0

Fig. 7. (a) Relative humidity interference analysis, (b) temperature interference analysis, (c) detection of volatile ammonia in fresh meat, (d) Pearson correlation analysis between temperature, humidity, and sensor performance.

3.4. Temperature and humidity compensation based on a BP neural network

BP neural networks, a type of multilayer feedforward neural network, have notable advantages in handling complex nonlinear fitting problems because of their unique architecture and learning algorithm [34]. The output y of the sensor is affected by temperature and humidity, resulting in frequency drift. To eliminate this offset error e, the model must estimate and correct it, thereby obtaining the compensated ideal output $\hat{y}$. Specifically, the actual output of the sensor can be expressed as the sum of the ideal output and the offset error.

$$y = \hat{y} + e \qquad (9)$$

To train the temperature and humidity compensation model, an appropriate loss function is required to measure the difference between the predicted output of the model and the actual output of the model. A commonly used loss function is the mean squared error (MSE), which helps the model to be continuously optimized by decreasing the error but increasing the prediction accuracy. The MSE is defined as follows:

$$E(\theta) = \frac{1}{2}\sum_{i=1}^{N}(y_i - \hat{y}_i)^2 \qquad (10)$$

where $E(\theta)$ represents the loss function of the model, y_i denotes the actual output of sample i (with offset); $\hat{y}_i$ indicates the predicted output of the model for sample i (compensated output), and N represents the number of samples.

In this study, a BP neural network is employed to construct a nonlinear mathematical model that maps temperature and humidity to the zero-point frequency shift of the microwave sensor. The network parameters are trained using the Levenberg–Marquardt (L–M) algorithm, which is well-suited for optimizing nonlinear models due to its efficient convergence and adaptability.

$$h_0 = -(J^T \cdot J + \lambda \cdot I)^{-1} \cdot J^T \cdot e^{(k)} \qquad (11)$$

In the equation, h_0 represents the correction increment, $J^T \cdot J$ denotes the second-order derivative matrix, I indicates the identity matrix, λ represents the damping factor, and $e^{(k)}$ denotes the iterative error.

Using the BP neural network fitting toolbox in MATLAB, parameter training was conducted via the L–M algorithm. The training set has a temperature range of 5–25 °C and a humidity range of 40%–80% and consists of 6280 samples. The test set has a temperature range of 0–30 °C and a humidity range of 35%–85% and consists of 7000 samples. The BP neural network comprises an input layer, a hidden layer, and an output layer, and *Sigmoid* and *Purelin* activation functions connect them. By adjusting hidden layer neurons and weights, complex nonlinear models can be accurately fit. The temperature and humidity were used as two input layer neurons, whereas the predicted zero-point frequency shift served as the output layer neuron (Fig. 8(a)). The final sensor output calibration effect achieved through the THBP is shown in Fig. 8(b). During validation, the correction regression results of the zero-point frequency shift of the sensor under temperature and humidity effects were analyzed. The correlation coefficients R of the training, test, and validation sets were greater than 0.969. These results strongly indicates that in the THBP, there is a highly significant linear correlation between the input variables (e.g., temperature and humidity) and the output variables (e.g., sensor-calibrated output).

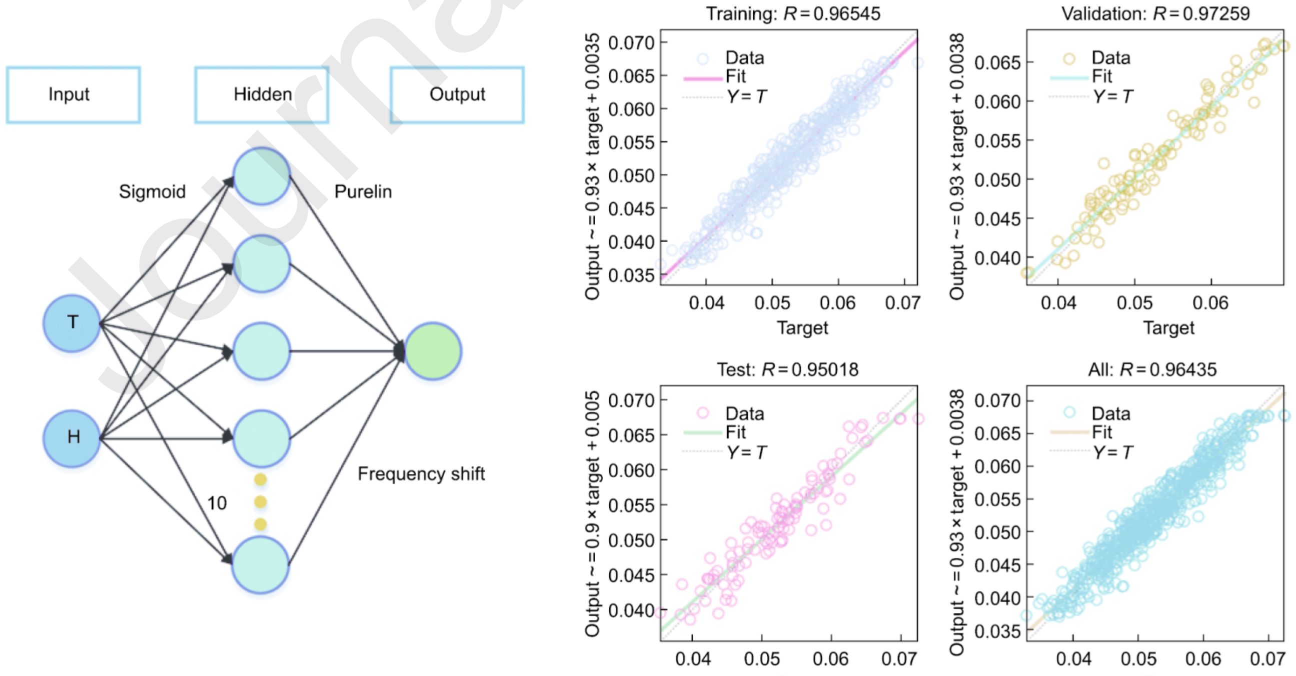

(a) (b)

Fig. 8. (a) Zero-frequency shift compensation model based on THBP compensation, (b) correlation coefficients of the training, testing, and validation datasets. *Y*: predicted value; H: humidity.

To validate the effectiveness of the temperature and humidity compensation model, the previously mentioned dataset was used as the training set, whereas a dataset collected using the same method from December 4 to December 10, 2024, was used as the test set to validate the compensation effect. To evaluate the THBP compensation model, its performance was compared with that of BP neural network-based temperature (TBP), random forest-based (RF), and SVM-based models (SVM). As shown in Fig. 9, both the TBP, RF, and SVM models slightly reduced the zero-point frequency shift, whereas THBP significantly suppressed drift fluctuations. When the mean and standard deviation were used as metrics (Table 1), all the models achieved some compensation effects, but THBP achieved the most stable results, reducing the drift to approximately 48 MHz (compared to the standard frequency drift of 45 MHz) and decreasing the fluctuation amplitude by 20%, increasing accuracy and reliability.

Table 1
Characteristics of zero-point frequency shift compensation for different models.

Model	Mean	Standard deviation	Mean deviation amplitude (MHz)
Original	0.05	0.027	60
TBP	0.04	0.020	55
SVM	0.35	0.017	53
RF	0.28	0.014	50
THBP	0.23	0.011	48

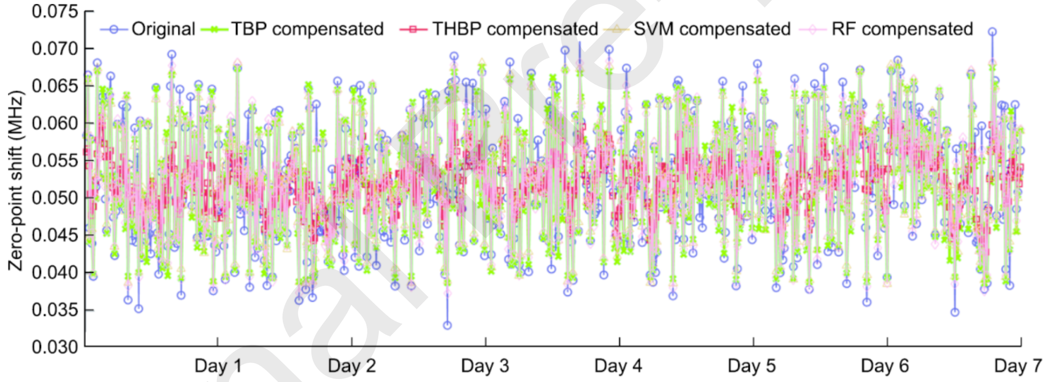

Fig. 9. Comparison of the performance of the zero-frequency shift compensation model.

3.5. Wireless monitoring of the quality of fresh meat

A nondestructive wireless detection system for monitoring meat spoilage based on a microwave antenna sensor is shown in Fig. 10(a). The system consists of a wireless transmission module and a reception module. The transmission module comprises a microwave antenna sensor and VNA that serves as the excitation source. The reception module includes a receiving antenna, a spectrum analyzer, and a display terminal such as a computer, smartphone, or tablet. When volatile ammonia compounds released during the spoilage of fresh meat in the reaction chamber are adsorbed onto the sensor surface, the VNA excites a radio frequency signal. This signal is modulated by the sensor and subsequently received by the receiving antenna, which is then transmitted to the spectrum analyzer. The data are ultimately analyzed via the terminal device, enabling wireless and non-destructive detection of meat quality deterioration.

The receiving antenna operates in the 2.1–2.3 GHz frequency range, and the receiver has a sensitivity of −80 dBm. When the ambient ammonia concentration changes, the resonance frequency of the microwave sensor shifts accordingly. This signal is then wirelessly transmitted to the receiver and ultimately displayed on the terminal device. In a wireless transmission system, factors such as distance and obstacles affect the received signal strength. Under free-space conditions, the received power P_R can be calculated as follows [35]:

$$P_R = \frac{\lambda^2 P_T G_{MGS} G_R}{16\pi^2 d^2} \qquad (12)$$

where λ represents the transmission wavelength, P_T denotes the transmitted power, G_R indicates the receiving antenna gain, and d represents the transmission distance. By combining Eqs. (5) and (12), the wireless microwave sensor model can be derived as follows:

$$\text{Conc.} = \frac{1}{a}\left(\frac{16\pi^2 d^2 P_R}{\lambda^2 P_T G_R} - b\right) \qquad (13)$$

On the basis of Eq. (13) and the spectral analyzer measurements, Fig. 10(b) shows that the concentration of volatile ammonia increases exponentially as the quality of fresh meat gradually deteriorates. The relationship between the received signal strength and transmission distance is shown in Fig. 10(c). As the distance increases, the received signal strength decreases. At a noise floor of −95 dBm, the transmission range of the wireless microwave sensor is 12 m.

To apply the sensor to meet the complex real-world requirements of meat cold-chain transportation, which is characterized by diversity and high fat content, this study examined the release characteristics of VOCs during the spoilage of different meats. Typical interfering gases generated from high-fat contents were specifically selected, and multiple gas concentration combinations were designed for testing to investigate the effects of various interfering gases on the accuracy of ammonia detection (Fig. 10(d)). Furthermore, for three representative meats (pork loin, beef loin, and chicken breast), the ammonia response percentages during spoilage were measured to analyze the species-specific interference effects of fat oxidation products on ammonia detection under different fat content conditions. As shown in Fig. 10(e), in chickens, the high-fat wing has the greatest response to ammonia, whereas the low-fat breast has the lowest response; in contrast, with response to pork and beef, the low-fat cuts have greater responses. This difference is attributed primarily to the volatile gases generated during fat degradation. High-fat portions release large amounts of volatile fatty acids and other organic compounds during spoilage, which dilute the local ammonia concentration and consequently reduce the response of the sensor to ammonia. In addition, the authors conducted an in-depth analysis of the impact of different packaging media on the stability of radio frequency signals. As shown in Fig. 10(f), because the radio frequency signals used in this study operate in the microwave frequency range, their propagation is relatively less affected by packaging materials such as plastic, cardboard, and acrylic. Consequently, the signals exhibit superior transmission stability under these conditions.

In practical applications, the microwave sensor is installed inside a reaction chamber located 5 m away from the receiving antenna. As the meat quality deteriorates, the receiving antenna captures variations in the signal of the sensor. The ammonia concentration is derived on the basis of the wireless microwave sensor model, and the temperature and humidity compensation module on the PC further corrects rectifies the readings (Figs. 10(g) and (h)). After compensation, the sensor sensitivity reaches 3.07 MHz·ppm^{-1}, and the error concentration is reduced to 0.06 ppm, increasing the ammonia detection accuracy by 31.11%.

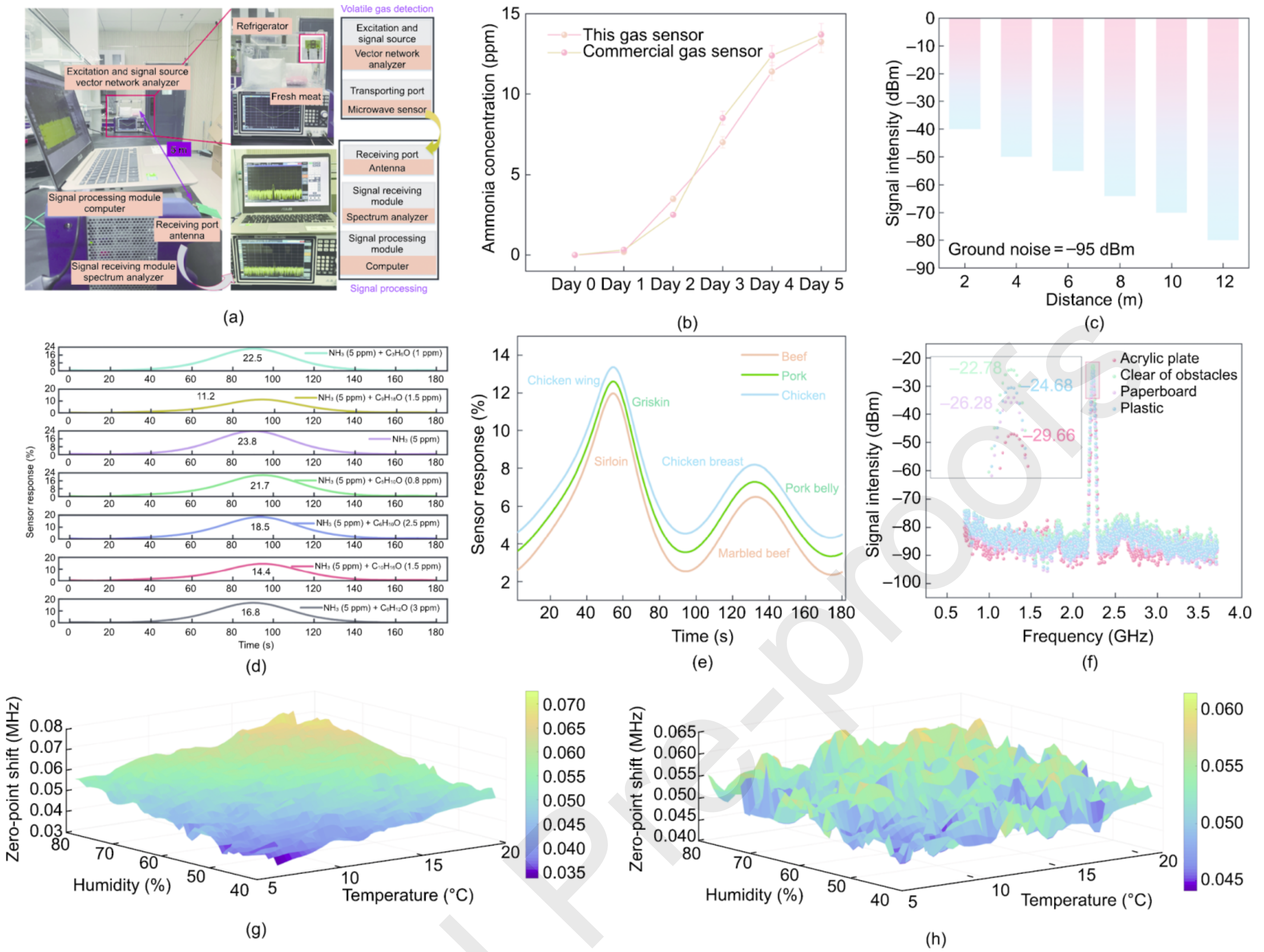

Fig. 10. (a) Wireless ammonia detection system, (b) sensor comparison test, (c) impact of wireless transmission distance on signal integrity, (d) analysis of cross-talk interference caused by volatile gases from high-fat meat spoilage, (e) percentage of ammonia cross-talk response in meats with varying fat contents, (f) effect of obstacle blockage on transmission signal, and comparison of 3D heatmap (g) before and (h) after temperature and humidity compensation.

4. Conclusions

To address frequency drift in MGSs caused by temperature and humidity fluctuations in complex environments, this study proposes a compensation algorithm that integrates Pearson correlation analysis with a BP neural network. This method enables effective modeling, analysis, and correction under various environmental conditions. Under low-temperature and high-humidity conditions, the sensor has advantages such as rapid response, short recovery time, high selectivity, excellent repeatability, and strong long-term stability. Compared with the TBP compensation model and the SVM-based temperature and humidity compensation model, the proposed approach achieves excellent compensation performance. The experimental results further reveal a distinct linear relationship between the radiation gain of the microwave sensor and the ammonia concentration. By incorporating a wireless transmission power model, a wireless microwave gas sensing system was developed, achieving high-precision wireless ammonia detection over a maximum range of 12 meters. This capability satisfies the requirements for detecting volatile ammonia associated with the quality deterioration of fresh meat during logistics, warehousing, and transportation. Future research will focus on further miniaturization of the sensing system, improved multi-gas discrimination capabilities, and deployment in various real-world supply chain environments to ensure comprehensive food safety and quality control.

Acknowledgment

This work was funded by the National Natural Science Foundation of China (62303018), supported by the Hefei Municipal Natural Science Foundation (HZR2413), and the University Synergy Innovation Program of Anhui Province (GXXT-2023-075).

References

[1] Sun C, Ge J, He J, Gan R, Fang Y. Processing, quality, safety, and acceptance of meat analogue products. Engineering 2021;7(5):674–8.

[2] Cole M, Augustin MA. Food safety and health. Engineering 2020;6(4):391–2.

[3] Ashiq J, Saeed U, Li Z, Nawaz MH. Advances in meat spoilage detection: a review of methods involving 2D-based nanomaterials for detection of spoiled meat. J Food Compos Anal 2024;132:106295.

[4] Xu J, Mu B, Zhang L, Chai R, He Y, Zhang X. Fabrication and optimization of passive flexible ammonia sensor for aquatic supply chain monitoring based on adaptive parameter adjustment artificial neural network (APA–ANN). Comput Electron Agric 2023;212:108082.

[5] Zhang J, Li Z, Yang H, Chen W, Wang Z, Zhou H, et al. Application of MXene composites for target gas detection in food safety. Food Chem 2024;460(Pt 2):140620.

[6] Sun Y, Yu G, Lu Q, Han H, Yang J, Xu Y. An electronic nose device with rapid and universal odor detection capability. Sens Actuators B Chem 2025;440:137871.

[7] Yang QY, Tan Y, Qu ZH, Sun Y, Liu AW, Hu SM. Multiple gas detection by cavity-enhanced Raman spectroscopy with sub-ppm sensitivity. Anal Chem 2023;95(13):5652–60.

[8] He W, Huang W, Wang Y, Li Z, Blanka T, Zhang X. A lamb freshness detection model using a flexible optoelectronic in-situ sensing system and multi-input multi-label causal ensemble learning. Food Chem 2025;471:142803.

[9] Hu Y, Tan Z. Enhanced ammonia-sensitive intelligent films based on a metal-organic framework for accurate shrimp freshness monitoring. Food Chem 2025;471:142805.

[10] Zhang L, Zhou M, Meng F, Bai J, Wang D, Tang M, et al. Recent advances in chemiresistive gas sensor for acetone detection: focus on room temperature. Trends Analyt Chem 2025;187:118213.

[11] Xue S, Jin Q, Wang X, Lu G. Microwave gas sensor based on differential planar resonator synergistically loaded with Pd-doped CdSnO3 for enhanced H2S detection. IEEE Electron Device Lett 2025;46(3):480–3.

[12] Lv W, Yang J, Xu Q, Mehrez JAA, Shi J, Quan W, et al. Wide-range and high-accuracy wireless sensor with self-humidity compensation for real-time ammonia monitoring. Nat Commun 2024;15(1):6936.

[13] Xu J, Yang X, Wang K, Jin Q, Wang X, Lu G. Confinement enrichment effect in HoMS-BaTiO3 microwave gas sensors for the detection of 10 ppb–0.55 v/v% ammonia at room temperature. ACS Sens 2024;9(4):2057–65.

[14] Zhang X, Zhu J, Cui T. An Ultracompact spoof surface plasmon sensing system for adaptive and accurate detection of gas using a smartphone. Engineering 2024;35:86–94.

[15] Xue S, Ji Y, Xu J, Zhang N, Wang K, Jin Q, et al. Electromagnetic enhanced microwave gas sensor for room temperature detection of ammonia. IEEE Trans Instrum Meas 2024;73:2001411.

[16] Lei Yong J, Li P, He XL, Tong MS, Guo LT, Zhang YJ. Multifrequency microwave liquid identification sensor based on interdigital split ring resonators. IEEE Trans Instrum Meas 2025;74:1–10.

[17] Beniwal A, Ganguly P, Khandelwal G, Gond R, Rawat B, Li C. Additive strategies to mitigate humidity interference effects on PEDOT:PSS sensors for ammonia detection. IEEE Sens J 2025;25(6):9357–66.

[18]Yi D, Zhang L, Wang Z, Wang L, Duan S, Yan J. Robust domain correction latent subspace learning for gas sensor drift compensation. IEEE T Syst Man CY-S 2023;53(12):7668–80.

[19] Mahdavi H, Rahbarpour S, Hosseini-Golgoo SM, Jamaati H. Reducing the destructive effect of ambient humidity variations on gas detection capability of a temperature modulated gas sensor by calcium chloride. Sens Actuators B Chem 2021;331:129091.

[20] Ji H, Zhu H, Zhang R, Zhang S, Yuan Z, Meng F. Semiconductor sensor virtual array: gas detection strategy in internet of things to suppress humidity interference. IEEE Internet Things J 2024;11(3):4934–41.

[21] Cheng Z, He G, Liang C, Dong Y, He W, Hou N, et al. The WOA-LSSVM temperature compensation technology for carbon nanotube-based ionizing gas. IEEE Sens J 2024;24(21):35212–20.

[22] Yuan Z, Sun H, Ji H, Meng F. Single feature to achieve gas recognition: humidity interference suppression strategy based on temperature modulation and principal component linear discriminant analysis. Sens Actuators B Chem 2025;423:136842.

[23] Naqui J, Fernandez-Prieto A, Duran-Sindreu M, Mesa F, Martel J, Medina F, et al. Common-mode suppression in microstrip differential lines by means of complementary split ring resonators: theory and applications. IEEE Trans Microw Theory Tech 2012;60(10):3023–34.

[24] Tanaka K, Cheng G, Nakamura T, Hiraoka K, Tabata H, Kubo O, et al. NH3 gas sensors based on single-walled carbon nanotubes interlocked with metal-tethered tetragonal nanobrackets. ACS Appl Nano Mater 2024;7(11):13417–25.

[25] Zhang J, Maimaitiyiming X. Study on phenyl series of polymers wrapping of different diameters of semiconducting single-walled carbon nanotubes for ammonia gas sensors. Sens Actuat B Chem 2024;405:135278.

[26] Chen LF, Ong CK, Neo CP, Varadan VV, Varadan VK. Microwave electronics: measurement and materials characterization. Chichester: Wiley; 2004. p. 254–60.

[27] Sun H, Cao M, Zhang P, Tian X, Lu M, Du L, et al. Magnetic-field-enhanced H2S sensitivity of Cu2O/NiO heterostructure ordered nanoarrays. ACS Sens 2022;7(7):1903–11.

[28] Hu G, Shi G, Li K, Ding D, Wu W, Tang X. Passive RFID sensor based on loaded short circuit and parasitic unit for ammonia sensing enhancement. Sens Actuators A Phys 2025;382:116167.

[29] Krudpun W, Chudpooti N, Lorwongtragool P, Seewattanapon S, Akkaraekthalin P. PSE-Coated interdigital resonator for selective detection of ammonia gas sensor. IEEE Sens J 2019;19(23):11228–35.

[30] Matindoust S, Farzi G, Nejad MB, Shahrokhabadi MH. Polymer-based gas sensors to detect meat spoilage: a review. React Funct Polym 2021;165:104962.

[31] Ren Z, Cui B, Cheng L, Jin J, Liang Y, Xue X, et al. Temperature and humidity effects on SAW hydrogen sensor and compensation method. IEEE Sens J 2024;24(14):22317–25.

[32] Liu C, Duan Z, Zhang B, Zhao Y, Yuan Z, Zhang Y, et al. Local Gaussian process regression with small sample data for temperature and humidity compensation of polyaniline-cerium dioxide NH3 sensor. Sens Actuat B Chem 2022;378:133113.

[33] Zhang S, Yuan Z, Liu Y, Meng F. Humidity-counteraction identification of VOCs driven by semiconductor sensor temperature modulation response data. IEEE Trans Instrum Meas 2024;74:9500509.

[34] Qi X, Chen G, Li Y, Cheng X, Li C. Applying neural-network-based machine learning to additive manufacturing: current applications, challenges, and future perspectives. Engineering 2019;5(4):721–9.

[35] Xuan X, Zhuang Z, Shi Q, Li H, Li C, Li M. Flexible antenna sensor based on vertical graphene for wireless humidity monitoring and IoT applications. IEEE Internet Things J 2024;11(10):18099–110.

Declaration of Interest Statement

☒ The authors declare that they have no known competing financial interests or personal relationships that could have appeared to influence the work reported in this paper.

☐ The author is an Editorial Board Member/Editor-in-Chief/Associate Editor/Guest Editor for this journal and was not involved in the editorial review or the decision to publish this article.

☐ The authors declare the following financial interests/personal relationships which may be considered as potential competing interests: